# Generalized liquid-based damping device for passive vibration control

Branislav Titurus[1]

*Department of Aerospace Engineering, University of Bristol, Queens Building, University Walk, Bristol, BS8 1TR, U.K.*

**This paper presents a liquid-based device with fluid-induced damping, stiffness and inertia effects. The proposed concept is modelled and experimentally studied. A lumped parameter fluid dynamics approach is used to model the flow-induced energy dissipation, inertia and volumetric compressibility. It is shown that the developed 5-state nonlinear dynamic model can be modified to represent a range of previously established models. A reference set of model parameters is determined from the calibration data obtained from a novel device demonstrator. The model's functional and parametric changes are shown to enable the device specializations which can approximate simpler as well as ideal devices such as dampers, springs and inerters. This work also demonstrates that the interaction between all three principal fluid effects opens routes to dynamic device tuning and frequency-selective damping.**

## Nomenclature

| | | |
|---|---|---|
| $A$ | = | cross-sectional area |
| $B$ | = | bulk modulus |
| B | = | effective damper stiffness factor |
| $b_L$ | = | equivalent mechanical inertance |
| $c_1, c_2$ | = | pressure-volumetric flow model coefficients |
| $c_L$ | = | laminar flow damping coefficient |
| $C_D$ | = | turbulent flow discharge coefficient |
| $F$ | = | force |
| $f_P$ | = | piston displacement frequency |
| $\mathbf{f}(\circ)$ | = | dynamic system model |

[1] Senior Lecturer, Department of Aerospace Engineering, University of Bristol, U.K.

| | | |
|---|---|---|
| $g_1, g_2, g_k$ | = | pressure-mass flow model coefficients |
| $k_D$ | = | equivalent mechanical stiffness |
| $l$ | = | channel length |
| $L$ | = | fluid inertance |
| $M$ | = | mass |
| $\mathbf{M}$ | = | dynamic system model mass matrix |
| $m$ | = | mass flow |
| $n$ | = | polytropic coefficient |
| $p, \Delta p$ | = | absolute pressure and pressure difference |
| $q$ | = | volumetric flow |
| $r_i(\circ)$ | = | pressure-sensitive density function |
| Re | = | Reynolds number |
| $S_t$ | = | geometric channel inertance factor |
| $T$ | = | time period |
| $t$ | = | time |
| $V$ | = | volume |
| $Y_P$ | = | piston displacement amplitude |
| $y$ | = | piston displacement |
| $X_0$ | = | volumetric fraction of air |
| $\alpha_j$ | = | positive real calibration multiplier |
| $\gamma$ | = | liquid to gas volume ratio |
| $\mu$ | = | dynamic viscosity |
| $\pi_k$ | = | exponent in the pressure-flow model |
| $\rho$ | = | fluid density |
| $(\dot{\circ})$ | = | time derivative |
| $\lvert\circ\rvert$ | = | absolute value |
| exp(∘) | = | exponential function |
| sign(∘) | = | signum function |
| $\partial$ | = | partial derivative |
| $R$ | = | subscript denoting “resistive” |
| $I$ | = | subscript denoting “inductive” |

## I. Introduction

Passive fluid-based systems represent a classical solution to many shock, motion, load and vibration control problems. From early military applications, they spread to aerospace, automotive and other industries. For instance, Duncan patented [1] a concept of the hydro-pneumatic shock absorber for aircraft landing in 1915 while a popular Houdaille-type automobile rotational liquid shock absorber was developed in 1920-ies [2]. In 1941, Igor Sikorsky used adapted shock absorbers to stabilize the blade lead-lag motions [3] in his VS-300 helicopter rotor [4]. During this and following periods, numerous types of devices were proposed, developed and applied to improve or enable performance of aerospace and other engineered systems.

The presence of energy dissipation, stiffness and inertial effects in fluid-based systems poses both challenge and opportunity. On the one hand, it is not straightforward to design, model and later control the parameters and properties of such systems. On the other hand, the insightful exploitation of all three phenomena allows refined performance tuning and novel designs which are unattainable when considering only the individual aspects of fluid behavior. Responding to varying functional requirements, while exploiting comparable physical phenomena, various classes of devices can be identified. Fluid-based dampers increase overall system damping by producing the motion-opposing forces through fluid flow throttling or shearing effects [5], [6], [7]. Additionally, semi-active forms of these devices with adjustable properties were studied extensively in recent decades [8], [9], [10]. Another class of devices provides spring capabilities by exploiting fluid compressibility and other pressure-driven volumetric effects in loaded systems of varying complexity and composition [11], [12], [13]. The next class is represented by shock absorbers where stiffness and damping properties are integrated in one system to provide passive and often directionally asymmetric control of shock responses while, usually, offering a long stroke functionality in spatially constrained designs. These types of devices are frequently used in automotive suspension and aircraft landing systems [14], [15], [16]. Like their damper counterparts, semi-active control capability was considered in shock absorbers too, e.g. [17].

A class of fluid-based devices which uses a combination of stiffness, damping and inertial properties can be used for dynamic tuning, vibration isolation and absorption [18]. There, resistance to changes in fluid motion conditions is the main driver behind induced inertial effects. The most widespread systems of this type are automotive engine mounts and suspension bushings [19], [20]. Historically, systems of this type can be traced to naval [21] and aerospace [22], [23], [24] applications. In this class too, semi-active designs, e.g. [24], and systems with advanced internal architectures, e.g. [25], were considered. Moreover, inertial and compressibility effects can be important in all fluid-based damping and spring system models, e.g. [26].

Other, more elementary systems such as frequency-sensitive dampers and purely acceleration-sensitive devices were studied as well. The principles of frequency-sensitive fluid flow phenomena were discussed in [27]. An early liquid-based concept was proposed in [28] as an alternative to the mechanical acceleration-sensitive flutter stabilization device [29]. Another aerospace application of mechanical acceleration-sensitive device combined with the kinematic liquid-based damping intensification was studied in [30]. Similar devices were studied more recently in the context of seismic protection [31], [32]. Owing to the presence of friction effects in laminar, turbulent and mixed flows, whether intended or not, all practical fluid-based realizations of pure acceleration-sensitive systems will feature damping. An effort to understand and exploit inertia-driven effects in mechanics influenced research in system analogies [27], vibration isolation [33], [34] and, recently, car suspension design [35]. A concept of a device sensitive to the relative acceleration across its two attachment ends was presented and systematically studied in [33]. Its mechanical realization, similar to a concept presented in [29], based on the translation to rotary motion transformation, was explored in the context of vibration problems in [31], [33]. A concept of an ideal acceleration-sensitive device, named inerter, was recently studied in the context of mechanical network synthesis [35] and its proposed fluid-based forms were researched in [36], [37], [38].

A baseline study for the present research is the work on semi-active fluid-based helicopter lead-lag dampers [10]. This work summarized the outcomes of the conceptual and experimental research [39], [40], [41]. The developed computational framework and experimental insights showed the importance and constraints arising from damper system dynamics. The importance of compressibility and its varying character was studied in [42]. Early insights on fluid inertia effects in dampers and shock absorbers were given in [26]. Current research aims to extend previous research by modelling and studying the combined effects of damping, stiffness and inertia arising from fluid mechanics [43]. One objective is to develop the low order physics-based nonlinear mathematical model which contains all three main physical effects at the comparable level of modelling fidelity. To support this effort, another objective is to develop a proof-of-the-concept laboratory demonstrator which features substantial dissipative, compressibility and inertial effects. A simple device topology is used to minimize the modelling uncertainty and maintain the links with the principal physical effects of interest. The broader motivation behind this research is the development of a scalable device model, with the corresponding operational insights, which can be used, with a good degree of confidence, for the range of aeroelastic performance and stability studies.

This research also intends to develop a suitable predictive platform for the class of concepts outlined in [21], [24], [28]. Those works provided limited insights into physics and the modelling assumptions while focusing either on their design or linear performance. More recent research [31], [32], conceptually similar to [29], studied

a combined hydro-mechanical design where the mechanical subsystem was the source of increased inertia. The first reported experimental results [38] confirmed previously anticipated dynamic behavior, e.g. [28], for this class of liquid-based devices. The present work extends the model [39] and it uses the modelling arguments from [46] aimed at maintaining continuity of the flows in the modelled systems. Similar modelling approach can be seen in use in automotive liquid mounts and bushings, e.g. [44], [45]. Here, a novel use of the constitutive compressibility law in its differential form is introduced and used to augment the pressure and flow state variables. Additionally, a modular frequency-sensitive damper design is proposed and implemented utilizing the design concepts from [41]. The 5-state nonlinear model is calibrated and then used to provide the insights associated with device specializations and its frequency-sensitive damping.

The paper is organized as follows: After an overview of the relevant concepts and published research, Section 2 introduces the studied system, its design and modelling principles. The main model of the device is discussed in Section 3 and Section 4 presents the case study which demonstrates the model's predictive capabilities and basic principles behind the device operation.

## II. System design and modelling principles

A typical liquid-based vibration control device consists of a mechanical and liquid subsystem. The mechanical subsystem transforms the applied structure-device interface deformations or displacements to the volumetric and pressure perturbations in the liquid subsystem. The net pressure-induced reaction loads applied at the structure-device interface influence dynamic response of the host structure. This research considers a basic two-chamber device configuration with a single interconnecting flow line or channel shown in Figure 1.

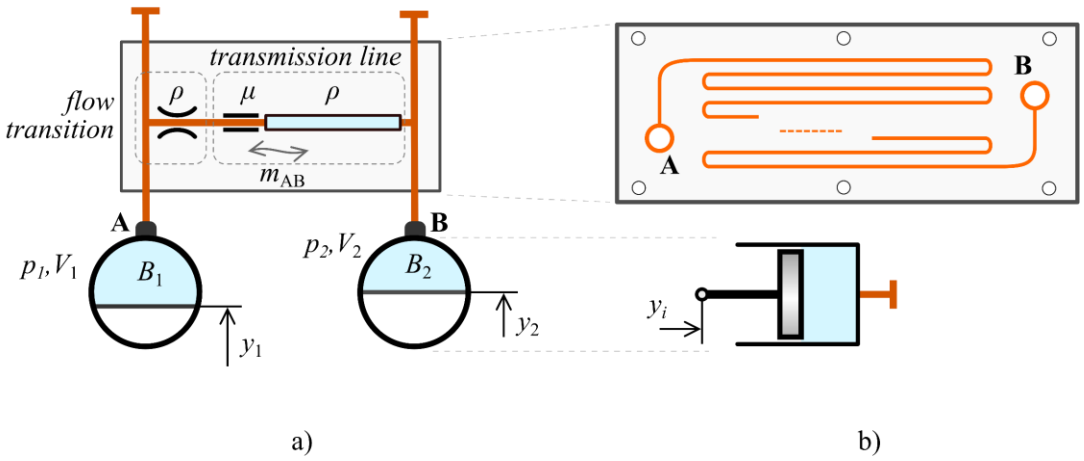


**Figure 1 Device architecture: a) general configuration, b) example component realizations.**

It is assumed that the chambers are modelled as the lumped volumes which contain a mixture of compressible liquid and air, the device works under isothermal working conditions, $T_r = const.$, and the channel flow is incompressible. The ports **A** and **B** represent a single inflow or outflow point for each volume. In general, the two independent input displacements $y_1, y_2$ produce changes in the volumes $V_1, V_2$ which then cause the mass flow $m_{AB}$ in the flow line. These changes further cause fluctuations in the chamber pressures $p_1, p_2$. The flow line, chamber properties and the applied displacements $y_1, y_2$ influence evolution of the pressures $p_1, p_2$. These pressures cause the reaction forces developed at the structure-device interface.

The model shown in Figure 1 uses the lumped physical parameters to characterize the flow transmission path. It combines a lumped parameter model of the flow transmission line [43], [47] with additional pressure loss sources [48]. The liquid viscosity $\mu$ is associated with resistive pressure losses due to internal fluid friction effects (such as those observed in the fully developed laminar flows). In the flow transmission model [43], the density $\rho$ is associated with the inductive pressure drop due to unsteady inviscid flows in the channel. Despite their inconsistency, the steady laminar and unsteady inviscid flow assumptions are commonly used to form a basic low frequency description of the flow dynamics in channels and ducts [47]. This model is further discussed in section III.B. Another source of the pressure losses which is associated with the fluid density originates from the resistive losses at inlets, outlets, bends and other flow irregularities which produce localized turbulent flows [48]. A final parameter which can be used in the flow line description is the fluid bulk modulus [49]. However, due to the line's assumed small volume, the corresponding compressibility effects are neglected in this study. The working volumes are the main source of compressibility effects through their effective bulk moduli $B_1, B_2$. Finally, the model shown in Figure 1a) does not predict the wave propagation phenomena and it is only suitable for the studies with the input frequencies significantly below the fundamental natural frequency of the flow line [43].

To obtain a flexible and modular design configuration, the fluid line is implemented as a channel machined in an aluminum plate. A computer controlled milling is employed to create the required channel feature. In this case, the channel is produced according to the conceptual sketch shown in Figure 1b). This channel introduces inertial effects to the system. One of the objectives of this research is to validate feasibility of this design concept. Figure 1b) also shows an example of the working volume. Such volume can be implemented, for instance, using a mechanical cylinder where additional compressibility effects can arise from the built-in accumulator or structural elasticity. Further design-focused discussion is presented in section IV.

## III. Device model

### A. Working volume dynamics

In general, the working volumes transform the imposed mechanical inputs, such as piston displacements, to the volumetric changes, fluid flows and pressure fluctuations. The rate of mass change in an open volume is $m \equiv \dot{M} = \dot{\rho}V + \rho\dot{V}$, where the dot is the time derivative, $\rho$ is the homogenized fluid (or liquid-gas) density, $V$ is the volume and $M$ is the total fluid mass in the volume. A constitutive compressibility relationship is used to establish the pressure state equation for a single volume. An isothermal tangential bulk modulus [49] in terms of density $B = \rho(\partial p / \partial \rho)_{T_r}$ [50], where $T_r$ is the reference temperature, is used for that purpose. After combining the time rate form of this constitutive pressure-density relationship with the previous mass change equation, the following pressure state equation can be written for an open working fluid volume

$$\dot{p} = \frac{B}{V}\left(-\dot{V} + \frac{m}{\rho}\right) \tag{1}$$

where $\dot{V}$ represents the time-dependent volume change and $m$ is the mass flow rate to or from the volume.
In the absence of additional compressible features, such as accumulators, the bulk modulus $B = B(p)$ usually represents the combined effect of the liquid-air or liquid-gas mixture. One suitable form of this function was developed by Gholizadeh [50]

$$B(p) = B_l \frac{1 - X_0 + X_0\left(\frac{p_0}{p}\right)^{1/n}}{1 - X_0 + B_l X_0 \frac{1}{n\,p}\left(\frac{p_0}{p}\right)^{1/n}} \tag{2}$$

where $B_l$ is the constant liquid bulk modulus, $X_0 = V_{g,0} / (V_{g,0} + V_{l,0}) = 1/(1+\gamma)$ is the volumetric fraction of air, $V_{l,0}$, $V_{g,0}$ represents the liquid and gas volumes at the reference (e.g. atmospheric) pressure $p_0$ and temperature $T_r$, $\gamma = V_{l,0} / V_{g,0}$ and $n$ is the polytropic coefficient.

This pressure-sensitive bulk modulus model of the liquid-gas mixture is specified for the assumed isothermal conditions, constant liquid bulk modulus and it has no capability to model gas or air dissolved in liquid. Gholizadeh [50] further showed, after introducing a consistent definition of the air fraction $X_0$, that this model is identical to other common bulk modulus models [49], [51]. Research [39] showed that a combination of the damping and compressibility phenomena introduces significant dynamic effects such as the delayed unsteady responses and spring-like behavior. It is shown in [40] that the simplified linear version of such damper model is

equivalent to the Maxwell viscoelastic unit. Research [42] showed that significant nonlinear compressibility effects can be modelled and useful insights can be obtained with the help of a basic single-state damper and pressure-sensitive bulk modulus models.

The assumption of compressible medium implies that the changes in its density need to be known to predict the pressure and flow dynamics in the system. Equation (1) describes evolution of the pressure variable $p(t)$. The liquid-air bulk modulus model (2) and the tangential bulk modulus definition are used here to form a differential constitutive pressure-density relationship. Assuming the constant bulk modulus, $B(p)=B_0=const.$, an explicit density relationship $\rho=\rho_0\exp(B_0^{-1}(p-p_0))$ can be written, where $\rho_0$ is the density at $p_0$. However, for the more general case, to avoid an integral expression $\int_{p_0}^{p} B^{-1}(p)\,dp$, the method proposed here uses the constitutive pressure-density equation in its differential form. Thus, the following relationship is used to compute the working volume density changes

$$\frac{1}{B}\dot{p}-\frac{1}{\rho}\dot{\rho}=0. \tag{3}$$

According to equations (1) and (3), the state of the lumped working volume is described by its pressure $p(t)$ and density $\rho(t)$. These two equations will be used to develop the model of the device.

**B. Flow line pressure drops**

The fluid subsystem considered here consists of the single flow channel where the incompressible lumped parameter mass flow model is used. It is assumed that the channel produces both inductive and resistive pressure changes [43]. The total pressure drop across the channel is $\Delta p=p_1-p_2=\sum_{(k)}\Delta p_k$, where $\Delta p_k$ are the constituent pressure drops. Considering the system topology, Figure 1a), the pressure drop is $\Delta p=\Delta p_R+\Delta p_I$, where $\Delta p_R,\Delta p_I$ are the resistive and inductive pressure drops, respectively. The chosen nonlinear power series model [16] of the overall resistive channel losses $\Delta p_R$ is

$$\Delta p_R=\text{sign}(m)\sum_{(k)} g_k\,|\,m\,|^{\pi_k} \tag{4}$$

where $k$, $g_k$, $\pi_k$ represent the contributing partial resistive pressure losses, $m$ is the mass flow rate. These parameters can be obtained through parameter identification, e.g. [40], when accurate modelling is required. Alternatively, for design purposes, they can be based on models of the Hagen-Poiseuille laminar flows; shearing viscous flows in narrow cavities and ducts [6]; formulations based on the Blasius correlation for turbulent flows

[16]; Darcy–Weisbach equation for mixed flows; energy and Bernoulli equations for losses at inlets and outlets [48]; etc.

This study uses the linear-quadratic model where $\pi_1 = 1$ and $\pi_2 = 2$ [16], [40]

$$\Delta p_R = g_1 m + \text{sign}(m)\, g_2 |m|^2 \tag{5}$$

and $g_1, g_2$ depend on the liquid physical and channel geometric properties.

In Figure 1, a discrete element which represents the overall inductive properties of the channel is connected in series with the resistive elements. This lumped parameter model, e.g. [43], [47], [52], is applied here. The corresponding pressure change is $\Delta p_I = L_e \dot{q}$, where $L_e = \rho l_{te} / A_{te}$ is the fluid inertance, $q$ is the volumetric flow rate, $\rho$ is the fluid density, $l_{te}, A_{te}$ is the effective length and cross-section, respectively, of the channel. Assuming the constant fluid density across the channel, the corresponding mass flow relationship is $\Delta p_I = S_t \dot{m}$, where $S_t = l_{te} / A_{te}$ is the channel inertance factor and $m = \rho q$ is the mass flow rate. Then, the total pressure drop is

$$\Delta p = S_t \dot{m} + g_1 m + \text{sign}(m)\, g_2 |m|^2 . \tag{6}$$

Equation (6) represents the basic model of the channel flow dynamics. It relates the pressure drops with the mass flows in the channel. This model can be used for low frequency conditions with the input frequencies significantly lower than the fundamental natural frequency of the flow line [43], [47]. To obtain the initial performance of the device, an assumption is made where $l_{te} = l_t$, $A_{te} = A_t$ and $l_t, A_t$ are the measured channel parameters. Further model improvements can be achieved using experimentally identified model parameters, e.g. [40], [42]. Alternatively, other refinements can utilize higher fidelity flow models, for example, those based on the relaxed assumptions pertaining the specifics of the cross-sectional flow rheology, [53].

### C. System equations

Using the concepts presented above, a mathematical model for the final device configuration, Figure 2, is developed in this section. This configuration can represent a symmetric double-acting cylinder which is often used to transform applied mechanical displacements to device flows. The two fluid volumes shown in Figure 1 are coupled such that $y_1 = -y_2 = y_P(t)$ and $y_P$ is the prescribed piston displacement. To ensure the mass conservation in the system with the incompressible channel flow, the outflow from volume 1 is denoted $-m_{12}$ and the corresponding inflow to volume 2 is $+m_{12}$, where $m_{12}$ represents the flow between volumes 1 and 2.

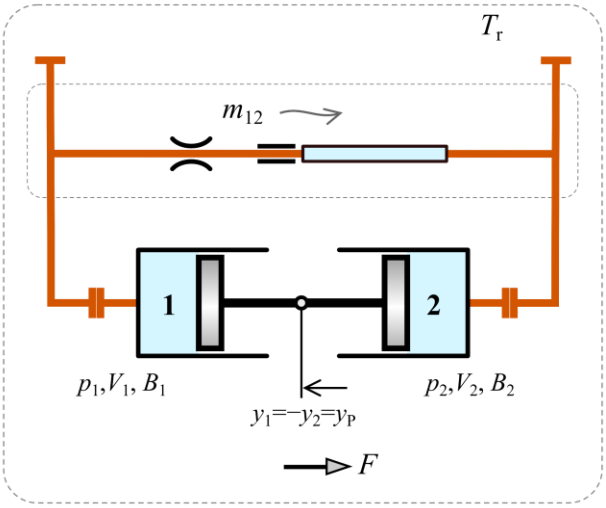


**Figure 2 Assembled system with a single flow channel and two working volumes.**

Further, to ensure the complementing and symmetric volumetric performance, the working volume changes are $V_1 = V_{0,1} - A_P y_P$ and $V_2 = V_{0,2} + A_P y_P$, where $V_{0,i}$ is the initial volume, $A_P$ is the wetted piston area. In line with equation (1) and the assumptions stated in this section, the pressure evolution equations are

$$\begin{aligned} \dot{p}_1 &= \frac{B_1(p_1)}{V_1(y_P)}\left( A_P \dot{y}_P - \frac{m_{12}}{\rho_1} \right), \\ \dot{p}_2 &= \frac{B_2(p_2)}{V_2(y_P)}\left( -A_P \dot{y}_P + \frac{m_{12}}{\rho_2} \right) \end{aligned} \tag{7}$$

where the subscripts 1, 2 refer to the individual fluid volumes; $B_i, V_i$ are functions of $p_i$ and $y_P$, respectively. In order to fully describe the changes in the working volume states, equation (3) is expressed for each working volume and combined with equations (7). The density evolution equations for each working volume are

$$\begin{aligned} \frac{\dot{\rho}_1}{\rho_1} - \frac{\dot{p}_1}{B_1(p_1)} &= 0, \\ \frac{\dot{\rho}_2}{\rho_2} - \frac{\dot{p}_2}{B_2(p_2)} &= 0. \end{aligned} \tag{8}$$

The final component of the device's system description is the flow model between the working volumes. Equation (6) is written in the usual form $\dot{m}_{12} = g(m_{12}, \Delta p)$. Thus, the mass flow evolution equation is

$$\dot{m}_{12} = \frac{1}{S_t}\left( \Delta p - g_1 m_{12} - \mathrm{sign}(m_{12})\, g_2 \,|\, m_{12} \,|^2 \right). \tag{9}$$

Depending on the nature of the considered pressure loss models, the coefficients $g_k$ might use the density $\rho_{12}$ of the liquid flowing in the channel. The working volumes contain the compressible liquid-air mixture where the states are such that, in general, $[p_1, \rho_1] \neq [p_2, \rho_2]$. The usual sources of compressibility can be accumulators and localized air bubbles trapped in the system after its filling. It is assumed that the modelled incompressible channel flow is unaffected by these local effects and its density is approximated as $\rho_{12} = \rho_l$, where $\rho_l$ is the nominal density of the working liquid. Similar lumped parameter modelling considerations were discussed in [46]. An alternative approach could use the pressure loss models developed for pneumatics applications or more detailed distributed flows [43].

Equations (7), (8) and (9) constitute a complete model of the device. This model represents the device dynamics with the state vector $\mathbf{x} = [p_1, \rho_1, p_2, \rho_2, m_{12}]^T$ and is characterized by the following system of equations

$$\begin{bmatrix} \rho_1 V_1 B_1^{-1} & 0 & 0 & 0 & 0 \\ -B_1^{-1} & \rho_1^{-1} & 0 & 0 & 0 \\ 0 & 0 & \rho_2 V_2 B_2^{-1} & 0 & 0 \\ 0 & 0 & -B_2^{-1} & \rho_2^{-1} & 0 \\ 0 & 0 & 0 & 0 & S_t \end{bmatrix} \begin{bmatrix} \dot{p}_1 \\ \dot{\rho}_1 \\ \dot{p}_2 \\ \dot{\rho}_2 \\ \dot{m}_{12} \end{bmatrix} = \begin{bmatrix} \rho_1 A_P \dot{y}_P - m_{12} \\ 0 \\ -\rho_2 A_P \dot{y}_P + m_{12} \\ 0 \\ \Delta p - g_1 m_{12} - \mathrm{sign}(m_{12})\, g_2 \mid m_{12} \mid^2 \end{bmatrix}. \tag{10}$$

The initial conditions can be written as $\mathbf{x}_0 = [p_0, p_0, \rho_0, \rho_0, 0]^T$, where $p_0, \rho_0$ represent the initial or reference pressure and density, respectively. Equation (10) represents a nonlinear dynamic system and it is expressed in the standard form $\mathbf{M}(t, \mathbf{x})\dot{\mathbf{x}} = \mathbf{f}(t, \mathbf{x})$. The time-dependent function $y_P(t)$ represents the controlled system input. Neglecting friction and piston inertia, the system output can be modelled as the force $F \approx A_P \Delta p$.

**D. Selected special cases and their physical interpretation**

Model (10) can be specialized to represent some previously developed models of vibration control devices. Initially, inertial effects are neglected by assuming $S_t = 0$ and $\Delta p = \Delta p_R$. The resulting algebraic flow equation (4) or (5), can be solved numerically or analytically for given $\mathbf{x} = [p_1, \rho_1, p_2, \rho_2]^T$ and so $m_{12} = f(\mathbf{x})$. Then, the reduced order model can be written in the following form

$$\begin{bmatrix} \rho_1 V_1 B_1^{-1} & 0 & 0 & 0 \\ -B_1^{-1} & \rho_1^{-1} & 0 & 0 \\ 0 & 0 & \rho_2 V_2 B_2^{-1} & 0 \\ 0 & 0 & -B_2^{-1} & \rho_2^{-1} \end{bmatrix} \begin{bmatrix} \dot{p}_1 \\ \dot{\rho}_1 \\ \dot{p}_2 \\ \dot{\rho}_2 \end{bmatrix} = \begin{bmatrix} \rho_1 A_P \dot{y}_P - m_{12} \\ 0 \\ -\rho_2 A_P \dot{y}_P + m_{12} \\ 0 \end{bmatrix}. \tag{11}$$

Model (5) has an analytical solution $m_{12}=\text{sign}(\Delta p)(-g_1+(g_1^2+4g_2|\Delta p|)^{1/2})/(2g_2)$. Furthermore, when assuming a simpler compressibility model, no linear pressure losses and after some algebraic rearrangements, it can be shown that this model is the same as the full order damper model presented in [46].

Further specialization of model (11) can be achieved by assuming $B_i = const.$ Under this assumption, equation (3) can be solved for each working volume and $\rho_i = r_i(p_i)$, where $r_i(p_i) = \rho_{0,i}\, e^{B_i^{-1}(p_i - p_0)}$ is the explicit pressure-sensitive density function. The reduced set of the state equations forms the following system

$$\begin{bmatrix} \rho_1 V_1 B_1^{-1} & 0 \\ 0 & \rho_2 V_2 B_2^{-1} \end{bmatrix} \begin{bmatrix} \dot{p}_1 \\ \dot{p}_2 \end{bmatrix} = \begin{bmatrix} \rho_1 A_P \dot{y}_P - m_{12} \\ -\rho_2 A_P \dot{y}_P + m_{12} \end{bmatrix} \tag{12}$$

or, after inverting the reduced order matrix $\mathbf{M}(t,\mathbf{x})$, the model is

$$\begin{bmatrix} \dot{p}_1 \\ \dot{p}_2 \end{bmatrix} = \begin{bmatrix} V_1^{-1} B_1 (A_P \dot{y}_P - r_1^{-1}(p_1)\, m_{12}) \\ V_2^{-1} B_2 (-A_P \dot{y}_P + r_2^{-1}(p_2)\, m_{12}) \end{bmatrix}. \tag{13}$$

Equation (13) represents the 2-state damper model with the constant compressibility where the total mass is conserved by maintaining the mass flow continuity between the working volumes. This model is similar to damper models which use the volumetric flow rate equilibrium equations for individual working volumes

$$\begin{bmatrix} \dot{p}_1 \\ \dot{p}_2 \end{bmatrix} = \begin{bmatrix} V_1^{-1} B_1 (A_P \dot{y}_P - q_{12}) \\ V_2^{-1} B_2 (-A_P \dot{y}_P + q_{12}) \end{bmatrix}. \tag{14}$$

When comparing models (13) and (14), it can be seen that these models are identical if $r_1^{-1} m_{12} = r_2^{-1} m_{12}$. This condition, however, is not valid because, in general, $\rho_1 \neq \rho_2$. Therefore, the mass transferred between the working volumes of system (14) is not conserved. As a result, previous research, e.g. [46], explained that model (14) features non-physical responses such as the drifting states and negative pressures.

To circumvent this problem and because the net pressure applied to the piston is usually of interest, model (14) is reduced so that only the differential pressure state $\Delta p = p_1 - p_2$ is computed. The errors associated with the working volume coupling inconsistency are neglected in this model while only its differential characteristics are further studied, e.g. the approximate volumetric flow and induced $\Delta p$ between the working volumes. Subtracting the two equations in (14) gives the following model

$$\frac{d}{dt}\Delta p = \dot{p}_1 - \dot{p}_2 = \left(\frac{B_1}{V_1} + \frac{B_2}{V_2}\right)\left[A_P \dot{y}_P - q_{12}\right]. \tag{15}$$

Then, if the assumption of small piston displacements about the reference piston position is used, i.e. $V_i(t) \approx V_{i,0}$ , $i=1,2$ and, for instance, $V_{2,0}=V_{1,0}=V_0$ and $B_1=B_2=B_0$, the final reduced order damper model is

$$\frac{d}{dt}\Delta p = \frac{2B_0}{V_0}\left[A_P \dot{y}_P - q_{12}\right]. \tag{16}$$

Equation (16) was used to form a part helicopter lead-lag damper model in [54]. Models (15) and (16) are useful despite their limiting assumptions. These models use small numbers of states and they reveal the links with the underlying physics. For example, an assumption of purely laminar pressure losses, $q_{12}=c_1 \Delta p$, as well as negligible piston inertia and seal friction, $F_D = A_P \Delta p$, gives the Maxwell viscoelastic unit model $\dot{F}_D + T_D^{-1} F_D = k_D \dot{y}_P$ with the relaxation time $T_D = V_0/(2B_0 c_1)$ and $k_D = 2B_0 A_P^2 / V_0$. For the incompressible case where $B_0^{-1}=0$, the model of viscous dashpot is obtained $F_{D,c} = (A_P^2/c_1)\dot{y}_P$ or, alternatively, when the channel is closed, $c_1 = 0$, the resulting linear spring model is $F_{D,B} = (2B_0 A_P^2/V_0) y_P$. Model (15) and its variants are implemented in the helicopter aeromechanics simulation codes R150 [10], CRFM [55], RCAS [56].

Further analysis of model (10) is aimed at its inertia-sensitive specializations. In this analysis, it is assumed that the bulk moduli are constant, $B_i = const.$, and the inertance factor $S_t$ is not negligible. Similar to equation (12) , combining these assumptions with equation (10) gives the following model

$$\begin{bmatrix} V_1 B_1^{-1} & 0 & 0 \\ 0 & V_2 B_2^{-1} & 0 \\ 0 & 0 & S_t \end{bmatrix} \begin{bmatrix} \dot{p}_1 \\ \dot{p}_2 \\ \dot{m}_{12} \end{bmatrix} = \begin{bmatrix} A_P \dot{y}_P - m_{12}\rho_1^{-1} \\ -A_P \dot{y}_P + m_{12}\rho_2^{-1} \\ \Delta p - g_1 m_{12} - \mathrm{sign}(m_{12})\, g_2 \,|\, m_{12} \,|^2 \end{bmatrix}. \tag{17}$$

The differential pressure $\Delta p = p_1 - p_2$ and the previously discussed assumption $r_1^{-1} m_{12} = r_2^{-1} m_{12}$ can be used again for further model reduction. The resulting 2-state model is

$$\begin{bmatrix} \mathrm{B}^{-1} & 0 \\ 0 & L_t \end{bmatrix} \begin{bmatrix} \Delta\dot{p} \\ \dot{q}_{12} \end{bmatrix} = \begin{bmatrix} A_P \dot{y}_P - q_{12} \\ \Delta p - c_1 q_{12} - \mathrm{sign}(q_{12})\, c_2 \,|\, q_{12} \,|^2 \end{bmatrix} \tag{18}$$

where $\mathrm{B} = B_1 V_1^{-1} + B_2 V_2^{-1}$ is the effective damper stiffness factor, $L_t$ is the liquid inertance and $c_k$ are the coefficients of the pressure versus volumetric flow polynomial model [40].

Equation (18) can be converted to an algebraic model when assuming the presence of incompressible liquid, $\mathrm{B}^{-1}=0$. Then, for additional model specialization, it is assumed that $c_2 = 0$ and $F_D = A_P \Delta p$. After substituting the differentiated condition $A_P \ddot{y}_P = \dot{q}_{12}$ to the second equation of (18), the device force is

$$F_D = A_P^2 (c_1 \dot{y}_P + L_t \ddot{y}_P) = c_L \dot{y}_P + b_L \ddot{y}_P = F_{D,c} + F_{D,L} \tag{19}$$

where $c_L = c_1 A_P^2$ is the laminar or viscous damping coefficient and $b_L = L_t A_P^2 = \rho l_t A_P^2 / A_t$ is the effective fluid-induced inertance [38].

The final model simplification can be achieved when assuming an inviscid flow, i.e. $c_1 = 0$. Then, the force induced by the relative piston acceleration $\ddot{y}_P$ is

$$F_D \equiv F_{D,L} = b_L \ddot{y}_P . \tag{20}$$

Model (17) is analogous to the models used for hydraulic engine mounts and suspension bushing, e.g. [25], [44], [45]. Model (18) represents the extended form of the single-state damper model [10] augmented with an inertia-sensitive channel. Model (19) shows that the induced force caused by a liquid channel is equivalent to a damper and inerter connected in parallel. These insights offer useful perspective on alternative designs, suitable phenomenological models and equivalent mechanical representations. In particular, models (19) and (20), in combination with all their underlying assumptions, provide useful links between the ideal devices and their practical realizations.

## IV. Case study

This case study demonstrates the proposed model and basic device functionality. A laboratory device demonstrator is first introduced and then tested. To obtain a suitable computational reference configuration, the model is calibrated against the experimental data. After this, the calibrated model is used in the parameter specialization and dynamic performance studies.

### A. Device design

A double-acting cylinder is used to implement the concept shown in Figure 2. The resulting device architecture is provided in Figure 3a). Its physical implementation, which combines the cylinder and hydraulic manifold with the machined flow feature, is shown in Figure 3b).

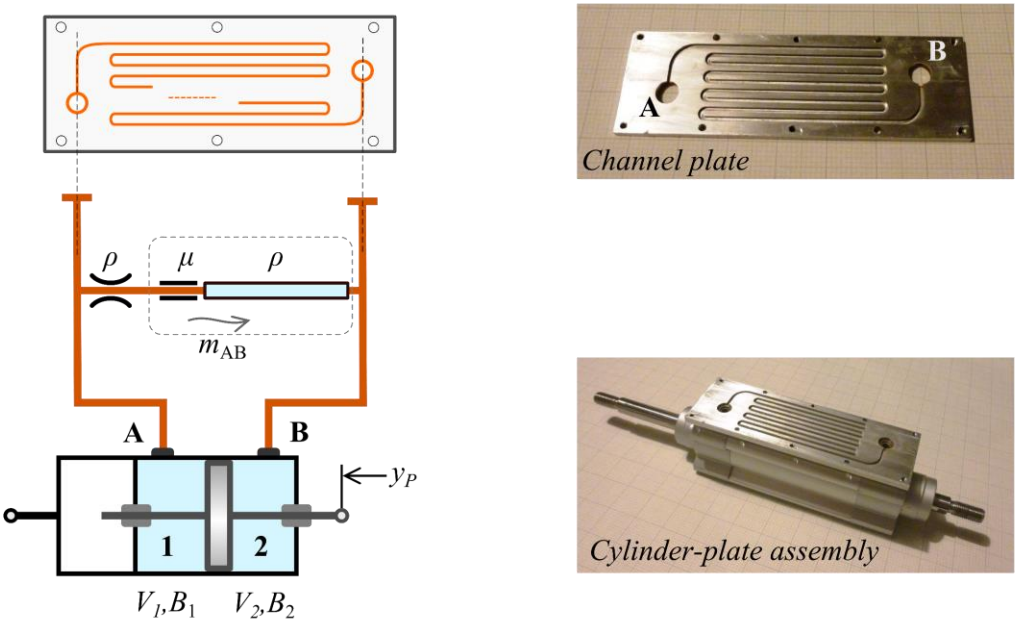


**Figure 3 Laboratory device demonstrator: a) model architecture, b) device prototype**

The total mass of the assembled and filled device is approximately $m_D = 1.2$ kg. An off-the-shelf symmetric double-acting DSBC series Festo cylinder with the internal bore diameter 32 mm, piston rod diameter 12 mm and the resulting wetted piston area 691.15 mm$^2$ is used. Its two fluid ports are connected to the manifold which consists of a pair of matched aluminum plates. To implement the desired inertial functionality CNC milling was used to machine the channel plate as shown in Figure 3b). The channel feature is 750 mm long and it has 2 mm × 2 mm cross-section. The liquid used is deionized water with the nominal density $\rho_l = 998.2$ kg/m$^3$ and dynamic viscosity $\mu = 8.9 \times 10^{-4}$ Pa.s. To simplify the design, this system is not externally pressurized during and after its filling. Consequently, during operation, pressures lower than the atmospheric pressure can be experienced. These conditions lead to suboptimal performance due to cavitation and possibility of increasing air contamination. Despite these limitations, this experimental configuration captures the key features of interest and provides sufficient support for model calibration. All the subsequent performance studies use this model with parameters at their reference or calibrated values.

### B. Test specification

A standard hydraulic machine, Instron 8800 with a 27 kN load cell, was used for testing. The device was placed in a load transfer frame and the load limits were set to $\pm 1$ kN. The load cell placed between a stationary

part of the device and an upper part of the test machine was used to measure loads while a Linear Variable Differential Transformer (LVDT) integrated in an actuated part of the test machine was used to record the actuator displacements at the sampling frequency of 200 Hz. Various influences were considered when processing the data: an initial electrical bias in the load cell was identified in the unloaded state and removed from the signal, an interface freeplay was minimized by attaching the frame directly to the machine grips, the piston inertia was not measured because the load cell was connected to the stationary part of the system operated in a motion-controlled mode, friction effects due to seal rubbing are briefly discussed in the following section. The motion control system harmonically excited the piston rod with the displacement waveform $y_P(t) = Y_P \sin(2\pi f_P t)$, where $Y_P$ and $f_P$ represent the amplitude and frequency, respectively. The piston velocities and accelerations were obtained from the measured displacements using a 21-point 4th order Savitzky-Golay Filter available in Matlab® [57].

### C. Model calibration

The aim behind the use of the proposed demonstrator is twofold. Firstly, it is used to obtain the data for model calibration. In this way, the reference model will be established for the following analyses. Secondly, by implementing and testing the proposed design, Figure 2, and later using the obtained measured data for model calibration, the proposed modular device architecture will be validated. The model parameters are summarized in Table 1. Their values are obtained directly from geometric measurements. The liquid and air properties correspond to their nominal values at room temperature, $T_r \approx 20\ ^\circ C$.

**Table 1 Device model parameters**

| *Parameter description* | *Units* | *Value* |
|---|---|---|
| Dynamic viscosity, μ | Pa.s | $8.9\times10^{-4}$ |
| Liquid density, $\rho_l$ | kg/m$^3$ | 998.2 |
| Liquid bulk modulus, $B_l$ | Pa | $1.5513\times10^{9}$ |
| Reference liquid volume, $V_{0,1}$, $V_{0,2}$ | m$^3$ | $1.7279\times10^{-5}$ |
| Wetted piston area, $A_P$ | m$^2$ | $6.9115\times10^{-4}$ |
| Channel area, $A_t$ | m$^2$ | $4.0\times10^{-6}$ |
| Channel length, $l_t$ | m | 0.75 |
| Liquid filling pressure, $p_0$ | Pa | 101325 |
| Polytropic coefficient of air, n | - | 1.35 |

Whilst not a performance-critical part of the concept, it is useful to discuss friction effects which occur in the system. These effects are assessed based on slow harmonic piston motion experiments. Figure 4 shows the measured responses at frequencies 0.25 and 0.5 Hz and amplitude 2 mm.

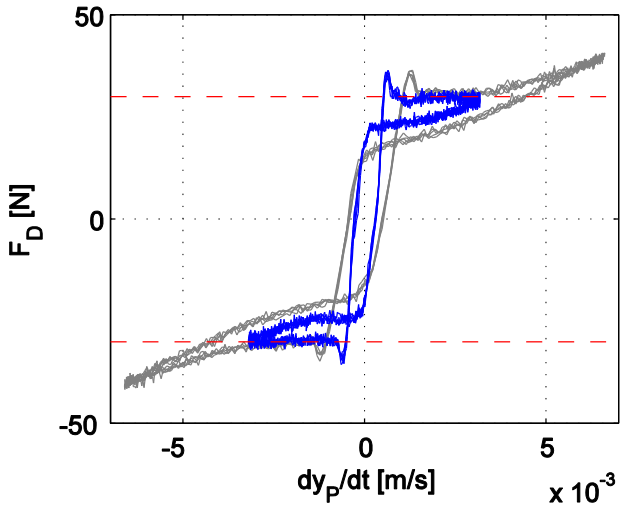


**Figure 4 Harmonic excitation test at 0.25 Hz and 0.5 Hz and 2 mm amplitude.**

In Figure 4, a pre-slide friction stage, associated with motion reversal, is followed by locally negative damping in the Stribeck region. After this stage, a nonlinear force increase and then a hysteretic unloading stage can be attributed to liquid and coupled liquid-friction effects. This sequence is repeated to complete the full response cycle. An increase in the excitation frequency leads to increasing hysteretic effects. The piston inertia force at this point is small with its peak values at approximately 1.8 N. The horizontal red dashed lines in Figure 4 indicate the representative friction force $|F_f| = 30$ N. Based on this value, only those experimental cases are considered in the following studies where friction constitutes the minor influence compared to the fluid effects. The predicted forces in this part of the paper are calculated using the basic relationship $F_D = A_P \Delta p + |F_f| \text{sign}(\dot{y}_P)$.

The unknown damping parameters are initially estimated assuming highly simplified flow conditions. The other uncertain parameter values are selected from within a realistic range. These parameters are then adjusted during the calibration to achieve a good agreement between the model and experimental responses. The volumetric fraction of air, $\gamma^{-1} = V_{g,0} / V_{l,0}$, is chosen to be 0.1 for both working volumes. Fully developed viscous flow in a straight conduit is used to estimate the initial coefficient $c_1$, where $c_1 = 8\pi\mu l_t / A_t^2$. Similarly, the channel entry and exit turbulent pressure losses [43] are used to obtain the initial $c_2$, where $c_2 = \rho_l / (2C_{D,e}^2 A_O^2)$ and $C_{D,e} = 0.48$ represents the combined entry and exit loss coefficient. These parameters are summarized in Table 2. The volumetric and mass flow coefficients are related such that $g_1 = c_1 / \rho_l$ and $g_2 = c_2 / \rho_l^2$. These calculations represent highly idealized and simplified flow conditions and the resulting parameter values constitute the starting

point for model calibration. It is expected that the calibrated pressure loss parameters will indicate more significant dissipation in the real system.

**Table 2 Initial and calibrated model parameters**

| *Parameter description* | *Units* | *Initial value* | *Calibration multiplier* |
|---|---|---|---|
| Volumetric fraction of air, $1/\gamma_1$ | - | 0.1 | 0.75 |
| Volumetric fraction of air, $1/\gamma_2$ | - | 0.1 | 1.22 |
| Laminar flow coefficient, $c_1$ | $kg.m^{-4}.s^{-1}$ | $1.0485\times10^{9}$ | 3.56 |
| Turbulent flow coefficient, $c_2$ | $kg.m^{-7}$ | $1.3539\times10^{14}$ | 4.04 |

The fluid-induced mechanical inertance is $b_L = 89.4$ kg and, therefore, the corresponding device inertance-to-mass ratio is $b_L / m_D = 74.5$. In line with standard hydraulic practice, e.g. [43], in this work, this parameter has a constant value in the tested frequency range. Model (10) is used together with parameters from Table 1 and Table 2. The responses are measured during harmonic piston excitation tests at the frequency-amplitude combinations [3 Hz, 3 mm] and [4 Hz, 2 mm]. These test cases are selected because they represent two sufficiently distinct characteristic profiles with responses significantly above the discussed friction levels. The first test case is used to calibrate the parameters in Table 2, where $p_{j,new} = \alpha_j p_{j,old}$, $\alpha_j$ is the calibration multiplier. The parameters $\alpha_j$ are determined such that the improved match between the measured and predicted responses is observed in the displacement-force and velocity-force domains. Results of the calibration are shown in Figure 5 and the multipliers are included in Table 2. The eight measured test cycles are shown to illustrate the periodic steady-state device behavior.

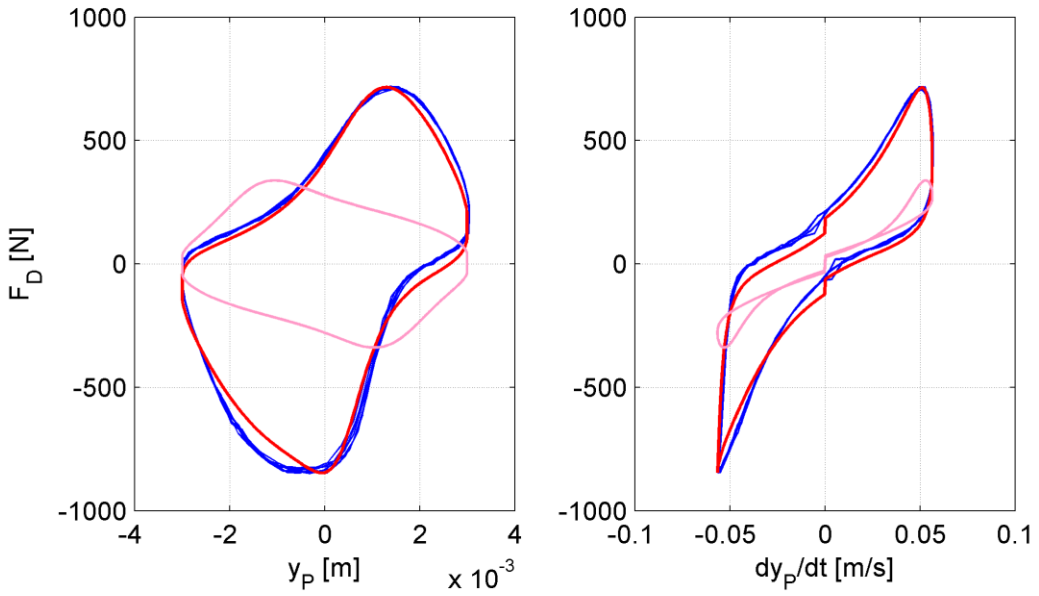


**Figure 5 Model calibration for the harmonic input at 3 Hz and 3 mm amplitude**

While initial predictions (pink lines) differ significantly from the measurements (blue lines), the calibrated model (red lines) indicates significantly improved match between the model and experiment. The main source of the final differences is associated with the zero-velocity friction-dominated regions. To account for this effect during the calibration, the Coulomb friction can be added to the computed pressure-dependent forces. This approach is applied in Figure 5. Unlike the abrupt modelled force transitions, the measured forces in this region change gradually. This observation suggests interactions between friction and fluid effects which are not studied here. The obtained results are in line with expected parameter uncertainty. The simplified device design and the filling procedure are responsible for the significant and asymmetric air contamination. The real flow conditions cause substantially increased levels of energy dissipation. The increase in the calibrated values of $c_1, c_2$ is associated with high flow velocity profile gradients near the channel walls during oscillatory flows [53] and with complex laminar-turbulent flow conditions caused by unavoidable geometric obstructions and irregularities.

To confirm the objectivity of the calibration process, an independent analysis is completed using the second data set. The results of this validation study are presented in Figure 6. The same presentation style is used to show the results. As before, the main difference is found in the zero-velocity regions which feature the gradual rather than the modelled abrupt force transition due to friction. However, overall, Figure 6 confirms that significant performance prediction improvement can be achieved when using the calibrated parameter values.

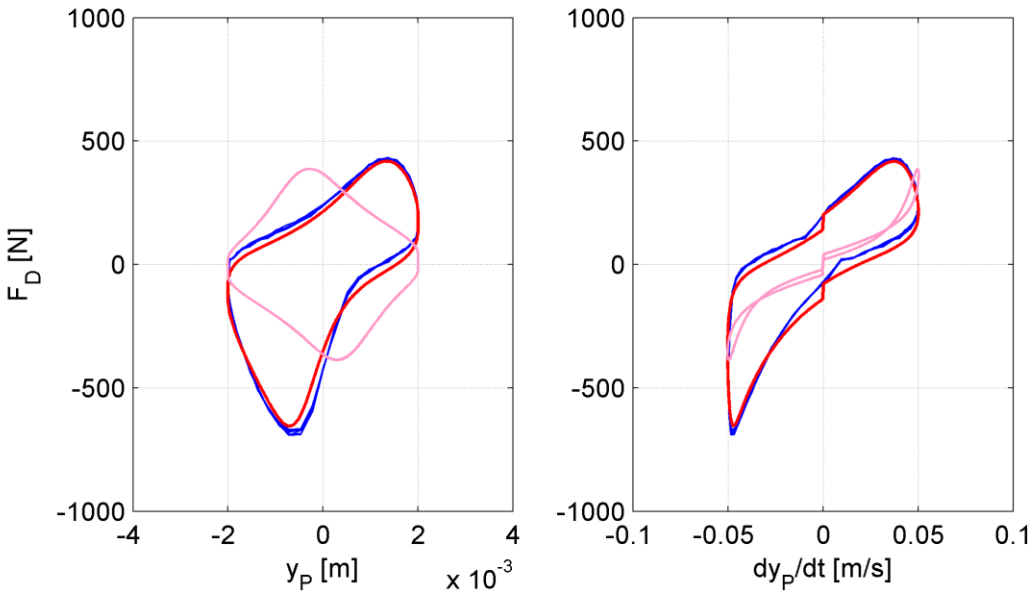


**Figure 6 Calibrated model validation with 4 Hz and 2 mm harmonic input**

Overall, a good agreement is achieved between the model and experiment. Equations (10) and its calibrated parameters in Table 2 provide the representative model of the device and its laboratory demonstrator. This model is used in the following parametric and performance studies.

### D. Device performance analysis

Initially, the model is studied using the parameter changes which produce the specialized stiffness, damping and inertia-dominated responses. This is achieved by changing the parameter values in model (10) while maintaining the model structure. This approach demonstrates the model's response range under parameter changes which can support an automated and systematic exploration across a wide range of device types in optimal design setting. After this, to illustrate the frequency-sensitive behavior, two model configurations are selected and explored across a range of the excitation frequencies. This study compares the generalized device responses with those corresponding to the standard liquid-based viscoelastic damper, e.g. [40]. The influence of nonlinearities is also briefly discussed.

The volumetric fraction of air is used to modify stiffness properties, the flow coefficients are used to change damping and the fluid inertance is used to influence inertial effects. Table 3 provides the summary of the applied parameter changes. The final parameter values can be obtained by applying the formula $p_{j,new} = \alpha_{j,2}\alpha_{j,1}\, p_{j,old}$, where $\alpha_{j,1}$ are the reference calibration multipliers and $\alpha_{j,2}$ are the specialization multipliers. All specialization studies are produced for the harmonic piston inputs with the frequency 3 Hz and amplitudes 1 and 3 mm. After

this, two additional parameter configurations specified in Table 3 are used to complete the dynamic performance comparison study.

**Table 3 Parameter multipliers for device studies**

| *Parameter* | *Units* | *Reference design* | *Specialized device* | | | *General device* | |
|---|---|---|---|---|---|---|---|
| | | | *Spring* | *Damper* | *Inerter* | *Device A* | *Device B* |
| $1/\gamma_1$ | - | 0.75 | 2.1 | 0.2 | $1.3\times10^{-4}$ | 2.0 | 2.0 |
| $1/\gamma_2$ | - | 0.75 | 2.1 | 0.2 | $1.3\times10^{-4}$ | 2.0 | 2.0 |
| $c_1$ | $kg.m^{-4}.s^{-1}$ | 3.56 | 10.0 | 1.0 | 1.0 | 0.3 | 0.3 |
| $c_2$ | $kg.m^{-7}$ | 4.04 | 10.0 | 1.2 | 1.0 | 0.3 | 0.3 |
| $S_t$ | 1/m | 1.00 | 0.1 | 0.1 | 7.0 | 1.8 | 0.1 |

Figure 7 to Figure 9 show the results of the specialization studies. All figures include the reference case based on the adjusted calibrated parameters (see reference design in Table 3), shown as gray lines. The corresponding ideal behavior is shown as red lines. All three subplots in each figure contain two blue curves which represent the computed responses when using 1 and 3 mm excitation. In addition to the usual force versus piston displacement and piston velocity diagrams, the force versus piston acceleration diagrams are included in each case to show the fluid inertia effects.

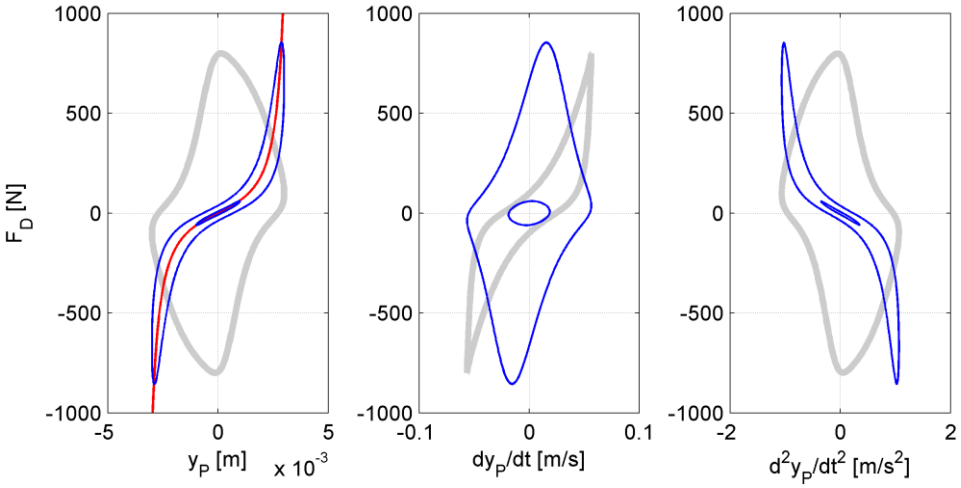


**Figure 7 Stiffness-dominated responses**

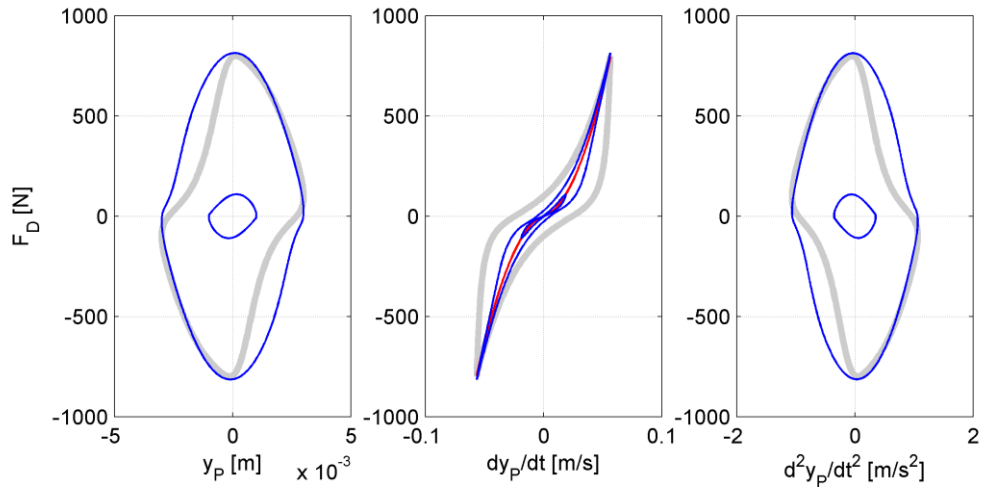


**Figure 8 Damping-dominated responses**

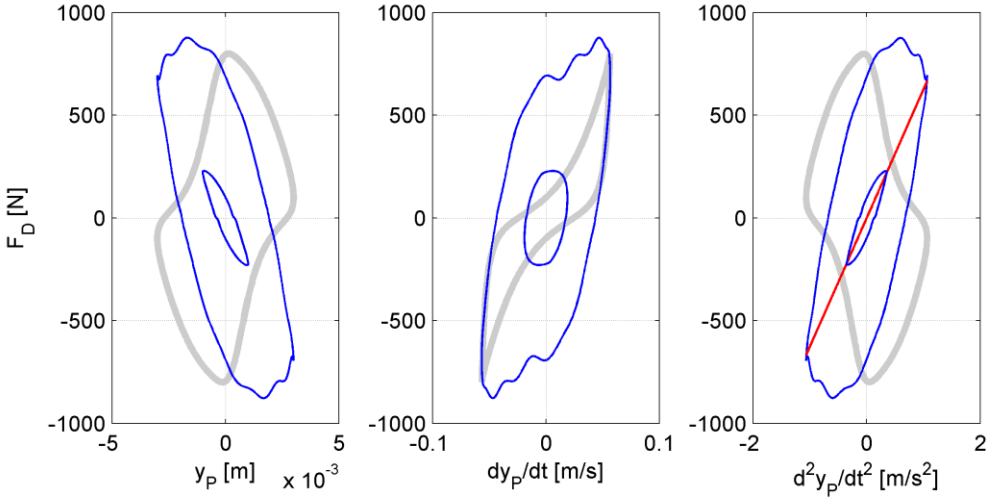


**Figure 9 Inertia-dominated responses**

Figure 7 contains the results of the spring specialization study. To achieve this, the model uses substantially increased flow resistance, decreased flow inertance and increased volumetric fraction of air. The two excitation cases and an ideal pneumatic spring characteristic help to show the effects caused by the nonlinear liquid-gas compressibility. These responses are shown in the velocity and acceleration domains as well. The velocity domain contains the response loops which are partially present in all its four quadrants. While not directly visible, it can be seen on further inspection that the response loops in this domain feature counterclockwise force-velocity changes with increasing time. This behavior is usually associated with steady-state response force lagging observed in stiffness-dominated systems.

Figure 8 shows the damper specialization study. To achieve this, the model uses reduced volumetric fraction of air and inertance while the flow resistance parameters are similar to the reference values. The two excitation

cases and an ideal damper characteristics help to show the effects caused by the nonlinear flow resistance. The area enclosed by the response loops in the displacement-force plot indicates significant energy dissipation in this system configuration.

Figure 9 presents the inertia-dominated responses. To generate this behavior, the model features significantly reduced volumetric fraction of air, unchanged flow resistance and the substantially increased inertance parameter. An ideal inerter and the two inertia-dominated response curves are presented in the acceleration domain. The velocity domain contains the response loops which are partially present in all its four quadrants. While not directly visible without further inspection, the response loops in this domain feature clockwise force-velocity changes with increasing time. This behavior is associated with the steady-state response force lead observed in inertia-dominated systems. The responses shown in the acceleration domain approximate the ideal linear inertance model. At the same time, locally transient and hysteretic effects can be observed in this domain due to a combined influence of the fluid compressibility and flow resistance.

The next study demonstrates a more complex frequency-sensitive device behavior. The responses for two different device configurations described in Table 3 are compared. The configuration with increased flow inertia, denoted Device A in Table 3, is studied in Figure 10. The configuration with reduced inertia and denoted Device B in Table 3 is then presented in Figure 11. A constant piston excitation amplitude of 1.5 mm is used together with the input frequencies of 1, 2, 4 and 7 Hz. These parameters are selected such that the key response features can be illustrated and discussed.

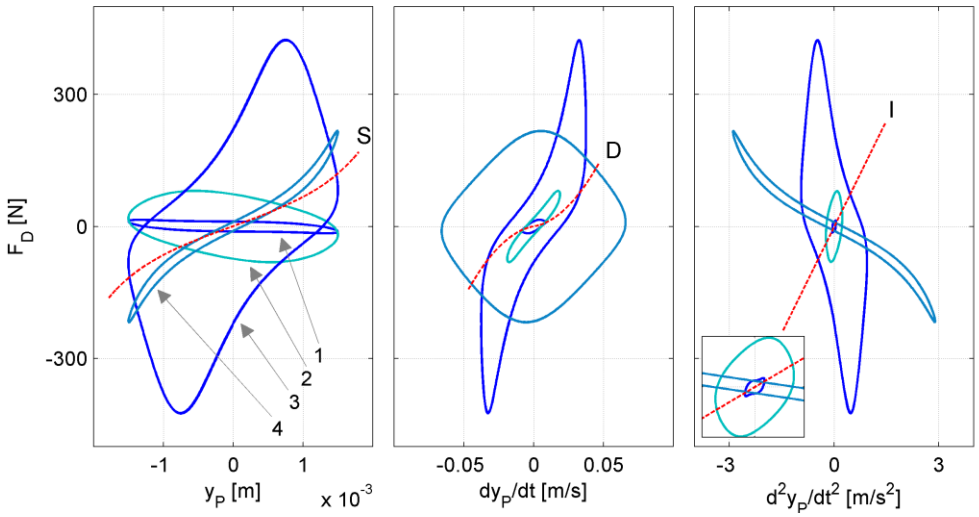


**Figure 10 Device A with increased flow inertia effects**

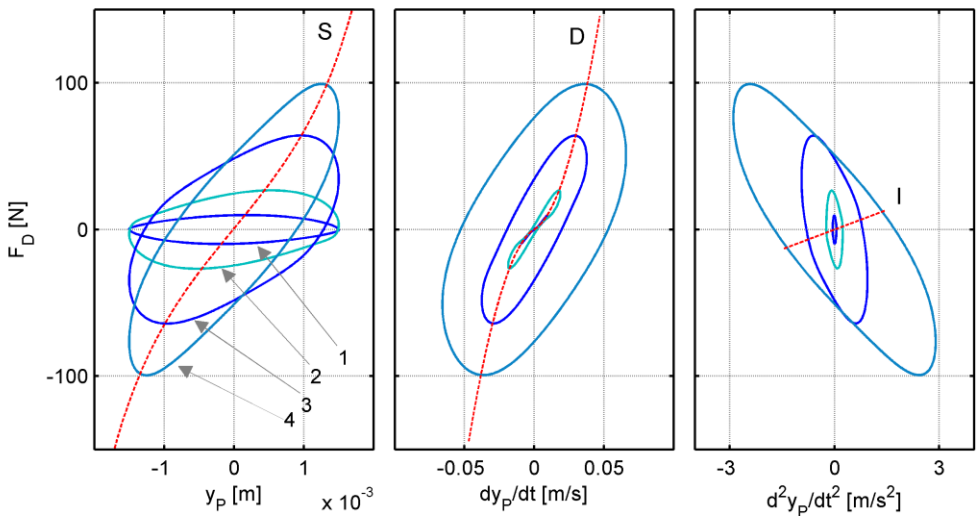


**Figure 11 Device B with reduced flow inertia effects**

All three characterization domains are presented in both studies. Red dashed lines indicate responses due to individual ideal effects of stiffness, damping and inertia without dynamic interactions. The steady state dynamic responses are computed for the excitation frequencies which produce inertia, damping and stiffness-dominated behavior. Different shades of blue and graph annotation are used to distinguish the computed responses.

Comparing Figure 10 and Figure 11, it can be seen that the system with increased fluid flow inertia features more complex responses in the excitation range. In Figure 10, inertia effects dominate the lowest frequency response (line 1). These responses are mainly present in the first and third quadrant of the acceleration-force domain. Increasing the excitation frequencies (lines 2 and 3) leads to increased presence of the dissipation effects. This is visible in the displacement-force domain where the corresponding response loops enclose increasing area, while the same responses shown in the velocity-force domain approximate the ideal nonlinear damping characteristics. Further increase in the excitation frequency (line 4) intensifies the volumetric variations in the device. This condition causes increased participation of the fluid compressibility in the device's responses. This effect can be observed in the displacement-force domain where the dynamic model approximates the ideal nonlinear spring. Consequently, the presence of the fluid inertia and compressibility in the device enables the frequency-sensitive, and therefore also frequency-selective, vibration control behavior [28]. In this way, through design and dynamic tuning, the fluid-based dissipation mechanism can be focused to influence selected regions of interest in the frequency domain. For case with reduced inertia effects, Figure 11, the system behaves as a traditional damper with compressible liquid [10]. As the peak loads increase with the increasing excitation frequencies, the initial damping-dominated responses change to the mixed viscoelastic and later stiffness-

dominated responses. These changes can be seen in the displacement-force and velocity-force domains when comparing the dynamic and ideal device responses.

Owing to the presence of the significant non-linear physical mechanisms, further understanding of this device can be developed using methods of nonlinear dynamic system analysis. Alternatively, to gain further understanding of the links with classical concepts such as tuned dynamic absorbers, various reduced order and linearized device models can be studied with the help of transfer function methods in the frequency domain.

## V. Conclusion

This research presents a detailed modelling study of the liquid-based vibration control device which can possess a balanced combination of fluid-based damping, stiffness and inertia properties. A detailed discussion of the modelling choices is presented. It is shown that the developed 5-state nonlinear dynamic model can be reduced, using various appropriate specialization assumptions, to represents a range of previously introduced vibration control device models. To establish a realistic reference parameter set, this model is successfully calibrated and assessed using the data collected during the experiments completed on the novel laboratory concept demonstrator. Using the established model and the calibrated parameter set, the key performance modes are discussed. It is shown that the model enables parametric modifications which can be interpreted as device specializations. The implications of such demonstration are theoretical, computational and practical. Suitable changes in the model parameters can alter the identity of the device significantly and enable optimal design under varying conditions or criteria. Furthermore, it is also shown that the device features frequency-sensitive and therefore frequency-tunable behavior. Consequently, such behavior opens the practical routes toward frequency-selective energy dissipation and vibration absorption. This capability is desirable in applications where classical liquid devices such as dampers produce excessive loads, for instance, at low frequencies associated with flight control subsystems.

## Acknowledgement

The laboratory demonstrator for this research was assembled and tested by Mr Ben Ward under the direction and guidance of Dr Titurus during his Final Year Research project in Spring 2016.

## References

[1] Duncan, T. S., “Improvements in or relating to the Landing Devices of Aeroplanes and Hydro-Aeroplanes,” British Patent No. GB191500568 (A), Published 13 April 1916.

[2] Shultz, A. B., and Casper, A. B., "Shock absorber," U.S. Patent No. 1,627,810 A, Filed 8 May, 1926, Published 10 May, 1927.

[3] … "The search for a solution" – The development of the VS-300 <149> Sikorsky helicopter design, *Proc. of the conf. "Diamond jubilee of powered flight: The evolution of aircraft design"*, 1978, Dayton, U.S.A. Doi: 10.2514/6.1978-3006

[4] Sikorsky, I. I., "Helicopter rotor control," U.S. Patent No. 2,517,509 A, Filed 9 May 1945, Published 1 Aug 1950

[5] Lee, D., and Taylor, D. P., "Viscous damper development and future trends," *The Structural Design of Tall Buildings*, Vol. 10, Issue 5, 2001, pp. 311-320. Doi:10.1002/tal.188

[6] Rittweger, A., Albus, J., Hornung, E., Öry, H., and Mourey, P., "Passive damping devices for aerospace structures," *Acta Astronautica*, Vol. 50, No. 10, pp.597-608, 2002. Doi: 10.1016/S0094-5765(01)00220-X

[7] Tarzanin, F. J., and Panda B., "Development and application of nonlinear elastomeric and hydraulic lag damper models," *36th Structures, Structural Dynamics and Materials Conference*, New Orleans, LA, U.S.A, Paper AIAA-95-1449, 1995, pp. 2534-2544.

[8] Crosby, M. J., and Karnopp, D. C., "The active damper – A new concept for shock and vibration control," *The Shock and Vibrations Bulletin*, Part 4, Prediction and Exp. Tech. in Isol. And Damp., June 1973, pp.119-133.

[9] Kordonsky, W., "Elements and Devices Based on Magnetorheological Effect," *Journal of Intelligent Material Systems and Structures*, January 1993, Vol. 4, No. 1, pp. 65-69. Doi: 10.1177/1045389X9300400108

[10] Titurus, B., "Vibration control in a helicopter with semi-active hydraulic lag dampers," *Journal of Guidance, Control, and Dynamics*, Vol. 36, No. 2, 2013, pp. 577-588. Doi:10.2514/1.56111

[11] Presthus, M., "*Derivation of Air Spring Model Parameters for Train Simulation*," Master's Thesis, Luleå University of Technology, 2002.

[12] Gao, B., Darling, J., Tilley, D. G., Williams, R. A., Bean, A., and Donahue, J., "Non-linear modelling of a gas strut used in ground vehicle suspensions," *Transactions of the Institute of Measurement and Control*, Vol. 29, Issue 2, June 2007, pp.159-183. Doi: 10.1177/0142331207070395

[13] Löcken, F., and Welsch, M., "The Dynamics Characteristic and Hysteresis Effect of an Air Spring," *Int. J. of Applied Mechanics and Engineering*, Vol. 20, No. 1, pp. 127-145, 2015. Doi: 10.1515/ijame-2015-0009

[14] Wahi, M. K., "Oleopneumatic shock strut dynamic analysis and its real-time simulation," *Journal of Aircraft*, Vol. 13, No. 4, 1976, pp. 303-308. Doi: 10.2514/3.44526

[15] Karam, W., and Mare, J.-C., "Advanced model development and validation of landing gear shock strut," *Proc. IMechE, Part G: J. Aerospace Engineering*, Vol. 224, 2010, pp. 575-586. Doi: 10.1243/09544100JAERO602

[16] Duym, S. W. R., "Simulation tools, modelling and identification, for an automotive shock absorber in the context of vehicle dynamics," *Vehicle System Dynamics*, Vol. 33, Issue 4, April 2000, pp. 261-285. Doi: 10.1076/0042-3114(200004)33:4;1-U;FT261

[17] Hong, S.-R., Wang, G., Hu, W., and Wereley, N. M., "Liquid spring shock absorber with controllable magnetorheological damping," *Journal of Automobile Engineering*, Vol. 220, No. 8, 2006, pp. 1019-1029. Doi: 10.1243/09544070JAUTO74

[18] Ormondroyd, J., and Den Hartog, J. P., "The theory of the dynamic vibration absorber," *Transactions of the American Society of Mechanical Engineers*, Vol. 50, 1928, pp. 9-22.

[19] Marzbani, H., Jazar, R.N., and Fard, M., "Hydraulic engine mounts: a survey," *Journal of Vibration and Control*, Vol. 20, No. 10, July 2014, pp. 1439-1463. Doi: 10.1177/1077546312456724

[20] Piquet, B., Maas, C. A., and Capou, F., "Next generation of suspension bushings: Review of current technologies and expansion upon new 3rd generation product data," Technical paper no. 2007-01-0850, April 2007. Doi: 10.4271/2007-01-0850

[21] Goodwin, A. J. H., "The design of a resonance changer to overcome excessive axial vibration of propeller shafting," *Institute of Marine Engineers Transactions*, Vol. 72, pp. 37-63, 1960.

[22] Braun, D., "Development of antiresonance force isolators for helicopter vibration reduction," in *Sixth European Rotorcraft and Powered Lift Aircraft Forum*, Bristol, U.K., September 16-19, Paper no. 18, pp. 1-17, 1980.

[23] Halwes, D. R., "LIVE - Liquid Inertia Vibration Eliminator," *36th Annual Forum of the American Helicopter Society*, Preprint No. 80-22, pp. 80-22-1 - 80-22-5, 1980.

[24] Margolis, D. L., "Semi-active fluid-inertia: A new concept in vibration isolation," *American Helicopter Society Northeast Region National Specialists' Meeting on Helicopter Vibration*, Hartford, Conn., November 2-4, 1981.

[25] Yang, C.-F., Yin, Z.-H., Shangguan, W.-B., and Duan, X.-C., "A Study on the Dynamic Performance for Hydraulically Damped Rubber Bushings with Multiple Inertia Tracks and Orifices: Parameter Identification and Modeling," *Shock and Vibration*, Vol. 2016, 2016, Article ID 3695950, 16 pages. Doi: 10.1155/2016/3695950

[26] Audenino, A. L., and Belingardi, G., "Modelling the dynamic behaviour of a motorcycle damper," *Proceedings of the Institution of Mechanical Engineers. Part D, Journal of Automobile Engineering*, Vol. 209, No. 4, 1995, pp. 249-262. Doi: 10.1243/PIME_PROC_1995_209_212_02

[27] Schönfeld, J. C., "Analogy of hydraulic, mechanical, acoustic and electric systems," *Applied Scientific Research, Section B*, Vol. 3, Issue 1, December 1954, pp. 417-450. Doi: 10.1007/BF02919918

[28] O'connor, B. E., "Inertia controlled flutter damper," U.S. Patent No. 2,742,113 A, Filed 17 Mar 1952, Published 17 Apr 1956.

[29] Bleakney, W. M., Zielinski, L. F., and Ede, C. M., "Flutter damper," U.S. Patent No. 2,471,857, Filed 9 May 1946, Published 31 May 1949.

[30] Hogan, W. H., "Shock absorber," U.S. Patent No. 2,856,179, Filed 22 Nov 1954, Published 14 Oct 1958.

[31] Arakaki, T., Kuroda, H., Arima, F., Inoue, Y., and Baba, K., "Development of seismic devices applied to ball screw: Part 1 Basic performance test of RD-series," *AIJ Journal of Technology and Design*, Vol. 5, No. 8 p. 239-244 June 1999, pp. 239-244. Doi: 10.3130/aijt.5.239_1 (in Japanese)

[32] Saito, K., Yogo, K., Sugimura, Y., Nakaminami, S., and Park, K., "Application of rotary inertia to displacement reduction for vibration control system," *13th World Conference on Earthquake Engineering*, No. 1764, Vancouver, Canada, 2004.

[33] Eliseev, S. V., "*Structural theory of vibration protection systems*," Nauka, Novosibirsk, Russia, 1978. (in Russian)

[34] Rivin, E. I., "*Passive Vibration Isolation*," American Society of Mechanical Engineers, 2003.

[35] Smith, M. C., "Synthesis of Mechanical Networks: The Inerter," *IEEE Transactions on Automatic Control*, Vol. 47, No. 10, 2002, pp. 1648-1662. Doi: 10.1109/CDC.2002.1184758

[36] Wang, F.-C., Hong, M.-F., and Lin, T.-C., "Designing and testing a hydraulic inerter," *Proceedings of the Institution of Mechanical Engineers, Part C: Journal of Mechanical Engineering Science*, Vol. 225, No. 1, 2011, pp. 66-72. Doi: 10.1243/09544062JMES2199

[37] Tuluie, R., "Fluid inerter," U.S. Patent No. 20130032442A1, Filed 25 Jan. 2010, Published 7 Feb. 2013.

[38] Swift, S. J., Smith, M. C., Glover, A. R., Papageorgiou, C., Gartner, B., and Houghton, N. E., "Design and modelling of a fluid inerter," *Int. J. of Control*, Vol. 86, No. 11, 2013, pp. 2035-2051. Doi: 10.1080/00207179.2013.842263

[39] Titurus, B., and Lieven, N., "Modeling and analysis of semi-active dampers in periodic working environments," *AIAA Journal*, Vol. 47, No. 10, October 2009, pp. 2404-2416. Doi:10.2514/1.41774

[40] Titurus, B., du Bois, J., Lieven, N., and Hansford, R. E., "A method for the identification of hydraulic damper characteristics from steady velocity inputs," *Mechanical Systems and Signal Processing*, Vol. 24, Issue 8, November 2010, pp. 2868-2887. Doi: 10.1016/j.ymssp.2010.05.021

[41] Titurus, B., du Bois, J., and Lieven, N., "Modeling and testing of a semi-active hydraulic damper in periodic working regimes," *AIAA Journal*, Vol. 50, No. 4, April 2012, pp. 844-854. Doi: 10.2514/1.J051152

[42] Titurus, B., "Complete semi-analytical damper model identification using triangular displacement inputs," *Proc. of the International Conference on Noise and Vibration Engineering ISMA 2014*, Leuven, Belgium, September 15-17, 2014, pp. 3179-3188.

[43] McCloy, D., and Martin, H. R., "*Control of Fluid Power: Analysis and Design*," 2nd (Revised) Edition, Ellis Horwood Limited, 1980.

[44] Kim, G., Singh, R., "A study of passive and adaptive hydraulic engine mount systems with emphasis on non-linear characteristics," *Journal of Sound and Vibration*, Vol. 179, Issue 3, 1995, pp. 427-453. Doi: 10.1006/jsvi.1995.0028

[45] Fredette, L., Dreyer, J. T., Rook, T. E., and Singh, R., "Harmonic amplitude dependent dynamic stiffness of hydraulic bushings: Alternate nonlinear models and experimental validation", *Mechanical Systems and Signal Processing*, Vol. 75, 2016, pp. 589-606. Doi: 10.1016/j.ymssp.2015.11.017

[46] Patten, W. N., Mo, C., Kuehn, J., and Lee, J., "A primer on design of semiactive vibration absorbers (SAVA)," *Journal of Engineering Mechanics*, Vol. 124, Issue 1, January 1998, pp. 61-68. Doi: 10.1061/(ASCE)0733-9399(1998)124:1(61)

[47] Morris, C. J., and Forster, F. K., "Oscillatory flow in microchannels. Comparison of exact and approximate impedance models with experiments," *Experiments in Fluids*, Vol. 36, 2004, pp.928–937. Doi: 10.1007/s00348-003-0776-9

[48] Akbari, M., Sinton, D., and Bahrami, M., "Pressure Drop in Rectangular Microchannels as Compared With Theory Based on Arbitrary Cross Section," *Journal of Fluids Engineering*, Vol. 131, 2009, 041202-1 - 041202-8. Doi: 10.1115/1.3077143

[49] Merritt, H. E., "*Hydraulic Control Systems*," John Wiley & Sons, New York, 1967, Chaps. 2, 3, 5.

[50] Gholizadeh, H., "*Modeling and Experimental Evaluation of the Effective Bulk Modulus for a Mixture of Hydraulic Oil and Air*," PhD Thesis, University of Saskatchewan, 2013.

[51] Cho, B.-H., Lee, H.-W., and Oh, J.-S., "Estimation technique of air content in automatic transmission fluid by measuring effective bulk modulus," *International Journal of Automotive Technology*, Vol. 3, No. 2, 2002, pp. 57-61.

[52] Lau, K. K., Edge, K. A., and Johnston, D. N., "Impedance characteristics of hydraulic orifices," *Proceedings of the Institution of Mechanical Engineers, Part I: Journal of Systems and Control Engineering*, Vol. 209, 1995, pp. 241-253. Doi: 10.1243/PIME_PROC_1995_209_392_02

[53] Fan, C., and Chao, B.-T., "Unsteady, laminar, incompressible flow through rectangular ducts," *Zeitschrift für angewandte Mathematik und Physik ZAMP*, Vol. 16, Issue 3, 1965, pp. 351-360. Doi: 10.1007/BF01591915

[54] Eyres, R. D., "*Vibration Reduction in Helicopters Using Lag Dampers*," Ph.D. Dissertation, Dept. of Aerospace Engineering, Univ. of Bristol, Bristol, England, U.K., Jan. 2005.

[55] Morales, R. M., Turner, M. C., Court, P., Hilditch, R., and Postlethwaite, I., "Force control of semi-active valve lag dampers for vibration reduction in helicopters," *IET Control Theory & Applications*, Vol. 8, Issue 6, 2014, pp. 409-419. Doi: 10.1049/iet-cta.2012.0397

[56] Kang, H., Floros, M. W., and Reddinger, J.-P., "Physics-Based Hydraulic Damper Model for Rotor Structural Loads," *Journal of Aircraft*, Vol. 53, No. 6, 2016, pp. 1697-1708. Doi: 10.2514/1.C033735

[57] Matlab, Software Package, Version 8.1, The MathWorks, Natick, MA, U.S.A., 2013.